Deciphering TADF Mechanisms in Metal-Free Organic Emitters BrA-HBI: Utilizing Optimally Tuned Range-Separated Functionals for Insight

Chunyue Yu(于春悦), Hang Yin(尹航)*, Jie Guo(郭婕), Wentian Zhang(张闻天), and Ying Shi(石英)*

Institute of Atomic and Molecular Physics, Jilin University, Changchun 130012, China

(Received 4 July 2024; accepted manuscript online 21 August 2024)

Metal-free organic emitters, characterized by their thermally activated delayed fluorescence (TADF) properties, offer considerable promise for the creation of highly efficient organic light-emitting diodes (OLEDs). Recently, Shao *et al.* presented a novel excited state intramolecular proton transfer (ESIPT) system BrA-HBI, demonstrating an emission quantum yield of up to 50% [*Adv. Funct. Mater.* **32**, 2201256 (2022)]. However, many open issues cannot be answered solely by experimental means only and require detailed theoretical investigations. For instance, what causes the activation of TADF from the Keto* tautomer and leads to fluorescence quenching in the Enol* form? Herein, we provide a theoretical investigation on the TADF mechanism of the BrA-HBI molecule by optimally tuned range-separated functionals. Our findings reveal that ESIPT occurs in the BrA-HBI molecule. Moreover, we have disclosed the reason for the fluorescence quenching of the Enol* form and determined that the T_2 state plays a dominant role in the TADF phenomenon. In addition, double hybrid density functionals method was utilized to verify the reliability of optimally tuned range separation functionals on the calculation of the TADF mechanism in BrA-HBI. These findings not only provide a theoretical reference for development of highly efficient organic light-emitting diodes, but also demonstrate the effectiveness of the optimally tuned range-separated functionals in predicting the luminescence properties of TADF molecules.

DOI: 10.1088/0256-307X/41/9/093301

Metal-free organic emitters, characterized by thermally activated delayed fluorescence (TADF), are pivotal in the development of displays, solid-state lighting, and time-resolved imaging.[1–5] In comparison to inorganic counterparts, these materials offer several advantages, notably higher luminous efficiency, reduced cost, and longer lifetime.[6,7] Upon photoluminescence, a small energy difference ($\Delta E_{\rm ST}$) and a large spin-orbit coupling (SOC) constants, between the first singlet (S_1) and triplet (T_1) excited states is essential to facilitate an efficient intersystem crossing (ISC) and reverse intersystem crossover (RISC) process that enables conversion of triple excitons to single excitons.[8–10]

Excited-state intramolecular proton transfer (ESIPT) has been demonstrated to facilitate the ISC/RISC process, thereby boosting the fluorescence quantum yield of TADF molecules.[8,11,12] ESIPT materials, characterized by metastable excited states resultant from the ESIPT mechanism, serve as excellent platforms for investigating ISC/RISC processes and transformations, facilitated by multiple intermediate states.[13–16] Plenty of studies have confirmed that the proton transfer process is important for increasing RISC efficiency between triplet and singlet states in ESIPT molecules, thereby facilitating TADF.[17]

Recently, Shao *et al.* presented a novel ESIPT system that is proposed to exhibit activation of TADF from the Keto* tautomer, and high fluorescence quantum yield was obtained.[1] In light of the intricate four-level photocycle, the (2′-hydroxyphenyl) benzimidazole (HBI) scaffold was chosen for its simplicity, augmented with Br to induce the intramolecular heavy atom effect.[1] They conducted intensive photophysical studies and obtained record high delayed emission quantum yield (QY). The designed ESIPT triplet emitters are expected to contribute to significant advancements in solid-state lighting, fluorescent probe, and photodynamic therapy in the future.[4,18–20] However, theoretical studies are needed for many open issues that cannot be solved solely through experimental methods. For instance, why is the activation of TADF from Keto* tautomer, while fluorescence quenching occurs in the Enol* form? What are triplet states that play a key role in the TADF phenomenon, and what are the mechanisms for the high utilization of triple state excitons? To improve our understanding of TADF mechanisms of metal-free organic emitters, we investigate TADF mechanisms of non-radiative transition processes based on research by Shao *et al.*[1]

Based on theoretical considerations, it is paramount to identify the optimal level of theory that strikes a balance between efficiency and accuracy in the prediction of electronic structure.[21] Given their substantial size, TADF molecules fall outside the scope of effective analysis using the post-Hartree–Fock (PHF) technique in their study.[21,22] Time-dependent density functional theory (TDDFT) is an authoritative method for exploring the excited states of extensive molecular systems.[23–26] This method achieves a pragmatic balance between computational precision and cost.[27,28] Unfortunately, the

*Corresponding authors. Email: yinhang@jlu.edu.cn; shi_ying@jlu.edu.cn
© 2024 Chinese Physical Society and IOP Publishing Ltd

conventional density functionals (such as global hybrid GGAs, global hybrid meta-GGAs)[29] often exhibit erroneous non-asymptotic behavior in their long-range domains. In evaluating donor-acceptor molecules that exhibit charge-transfer properties,[8] conventional density functionals used in TDDFT calculations often undervalue the excitation energies significantly.[30–32] The introduction of range-separated (RS) exchange density functionals has recently helped overcome the charge-transfer (CT) difficulties in TDDFT. In RS functionals, the following expression[33,34] for the inter-electron distance r_{12} separates the exchange terms into short-range domains and long-range domains, i.e.,

$$\frac{1}{r_{12}} = \frac{1-[\alpha+\beta\mathrm{erf}(\omega r_{12})]}{r_{12}} + \frac{\alpha+\beta\mathrm{erf}(\omega r_{12})}{r_{12}} \quad (1)$$

where ω, the range-separation parameter, signifies the reciprocal of the distance at which the exchange term changes from DFT characteristics to HF-like properties.[21] In range-separated functionals, the ω values exhibit strong system dependence, most notably in π-conjugated systems. Baer *et al.*[31] have proposed a non-empirical criterion for determining the optimal value of ω in RS functionals. Their strategy effectively addresses the damaging long-range self-repulsion common in many approximate DFT implementations.[31] The principle of "optimal tuning" entails the modification of ω to align with an essential requirement dictated by the accurate functional in the realm of exact Kohn–Sham (KS) or generalized KS (GKS) theory: For a system with N electrons, the inverse of the negative HOMO energy $-\varepsilon_H(N)$ is required to match the molecular vertical ionization potential (IP).[21,31] This method has proven to be effective in scenarios traditionally viewed as problematic for TDDFT. Furthermore, recent applications of the Tamm–Dancoff approximation (TDA) within TDDFT have reliably produced absorption and emission spectra, with significantly superior calculations of the singlet–triplet energy gaps essential to TADF systems.[21,35]

In this work, we decipher the TADF mechanisms of the metal-free organic emitters BrA-HBI by optimally tuned range-separated functionals. Concretely, in order to prove ESIPT properties of BrA-HBI molecule, we calculate molecules' configurations, frontier molecular orbitals (FMOs), potential energy curves (PECs), IR spectra. Fluorescence peaks and oscillator strength are also investigated. The calculations demonstrate that fluorescence quenching occurs in the Enol* form due to the fact that its oscillator strength is negligible. Furthermore, we determine the time scale of the proton transfer process for this molecule using the transition state theory. To investigate the fluorescence characteristics of the molecules, SOC constants, the energy gaps of the energy levels, the nonradiative decay rates and electron–hole distributions are also investigated. It is evident from the calculations that the T_2 energy level plays a key role in the collection of triplet state excitons. Furthermore, to demonstrate the validity of computing TADF phenomena at the ωB97X*/Def2-TZVP level, we employ the double hybrid density functionals method.[36–38] Our research not only contributes to the development of the TADF molecule, but also demonstrates the effectiveness of the optimally tuned range-separated functionals in predicting the luminescence properties of the TADF molecule.

Computational Methods. Calculations in our work were performed at the ωB97X*/Def2-TZVP level. As a result of this setup, we calculated the optimized geometric structures, emission properties, FMOs, IR spectra, and PECs using Gaussian 16[39] in the default configuration. Additionally, the SOC constants were calculated using PySOC in combination with Gaussian 16.[40,41] In MOMAP, the nonradiative decay rates between singlet and triplet states were also examined.[42–45] The single-triplet state energy level gaps were verified using double hybrid density functionals method at SCS-ωB2GP-PLYP/Def2-TZVP, SCS-ωPBEPP86/Def2-TZVP and SCS-ωB88PP86/Def2-TZVP level, respectively,[37] through the ORCA 5.0.4 software.[46]

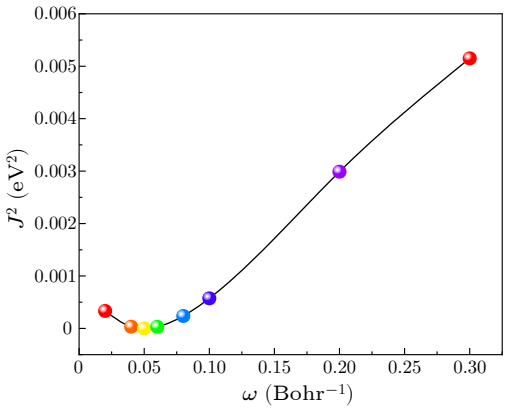

Fig. 1. J^2 of Eq. (1) versus ω for BrA-HBI, ωB97X functional. The optimal value determined from an interpolating function is $\omega* = 0.05\,\mathrm{Bohr}^{-1}$.

Tuning of the ωB97X Functional for BrA-HBI. For the BrA-HBI system, the ωB97X functional[47] underwent precise tuning by reducing J^2, as specified in the Supporting Information (SI). We optimized the ground state configuration and calculated it under the optimized configuration to further obtain the optimal tuning for the range-split parameter. The parameters calculated based on different forms are $0.050092\,\mathrm{Bohr}^{-1}$ (Enol) and $0.050231\,\mathrm{Bohr}^{-1}$ (Keto), respectively. It can be observed that the parameter values for the Enol and Keto forms are almost approximate in this system. In Fig. 1, the variation of J^2 values for BrA-HBI, corresponding to different ω values, is illustrated. The optimal ω^* value for BrA-HBI is $0.05\,\mathrm{Bohr}^{-1}$, which is much lower than the original value of $0.3\,\mathrm{Bohr}^{-1}$. According to recent theoretical research,[48,49] the default value of the ω parameter is too large, resulting in excessive electron localization. Our tuning approach achieves a balance between delocalization and localization in the BrA-HBI molecule. Hereafter, the functional that has been optimally tuned is referred to as ωB97X*.

Fluorescence Peak. The fluorescence peaks of BrA-HBI molecules were calculated at the ωB97X*/Def2-TZVP

level. Specifically, the fluorescence peak that derives from the Keto* structure was determined to be at 450 nm. The theoretical result is in agreement with the experimental data by Shao *et al.*,[1] demonstrating the reliability of our calculations. Additionally, we predicted the fluorescence peak of Enol* form at 410 nm. However, the fluorescence of the Enol* form was not observed in the experiment of Shao *et al.*[1] Further theoretical studies have demonstrated that the emission oscillator strength of the Enol* form is negligible, which quenches the fluorescence of the Enol* form for the BrA-HBI molecule.

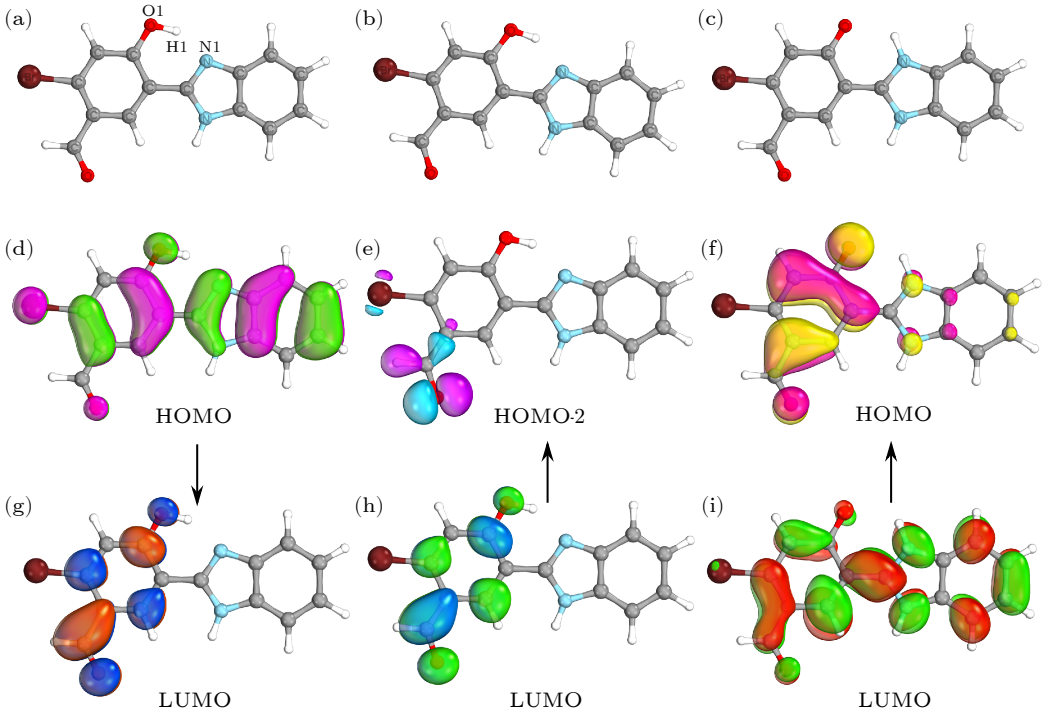

Fig. 2. Schematic plots of the optimized BrA-HBI structures and frontier molecular orbitals at the S_0 and S_1 states: Enol form (a), Enol* form (b), Keto* form (c); HOMO of the Enol form (d), HOMO-2 of the Enol* form (e), HOMO of the Keto* form (f), LUMO of the Enol form (g), LUMO of the Enol* form (h), LUMO of the Keto* form (i).

Verification of ESIPT Mechanism. To depict the ESIPT of BrA-HBI, geometric structures[50] for BrA-HBI molecules were optimized in S_0 (Enol), S_1 (Enol*), and S_1 (Keto*) form, depicted in Fig. 2. The corresponding geometric parameters were also calculated in Table S2. Combined with Fig. 2 and Table S2, it is obvious that the intramolecular hydrogen bonding (O1–H1$\cdots$N1) is formed in the Enol and Enol* form, whereas the intramolecular hydrogen bonding (O1$\cdots$H1–N1) appears in the Keto* form. It is deduced that during the reaction from Enol* form to Keto* form, the initial O1–H1 bond is broken and the N1–H1 bond is formed. Further, the BrA-HBI under investigation exhibits two stable structures in the excited state, which indicates that it undergoes ESIPT reactions upon excitation.

To examine the characteristics of the excited state, we analyzed the FMOs in different structures (Enol, Enol* and Keto*),[51,52] which are shown in Fig. 2. Specifically, the absorption process from Enol structure mostly corresponds to the transition from HOMO to LUMO. The fluorescence emission process of Enol* is primarily attributed to the transition from LUMO to HOMO-2. The fluorescence emission process mainly occurs to the transition from LUMO to HOMO in Keto* form. It is worth noting that the HOMO and LUMO (Enol form) are of π and π^* characters, respectively. This means that the S_1 state has $\pi\pi^*$ character, which promotes proton transfer.[53] On the other hand, by comparing the FMOs for the Enol* and Keto* forms of the BrA-HBI molecule, the extent of overlap between HOMO-2 and LUMO in the Enol* form was found to be weak. It can be demonstrated that the negligible oscillator strength in the Enol* form arises from the weak overlap of the FMOs.[54,55]

To further understand the ESIPT mechanism of the BrA-HBI molecule, PECs[56] for the S and S_1 states were scanned along the distance between O1 and H1 in Fig. 3. The S_1 state has two stable geometries located at approximately 1.0 Å (Enol* form) and 2.1 Å (Keto* form). When BrA-HBI is excited to the S_1 state, it exhibits two stable equilibrium geometries. The tautomer form at state S_1 can be achieved as follows: H1 transfers from O1 to N1 and forms the new hydrogen bond (O1$\cdots$H1–N1). The presence of the tautomer equilibrium geometry is powerful evidence for ESIPT with photoexcitation to the S_1 state.

IR spectra can analyze the formation and breaking of chemical bonds, which is used to describe the ESIPT process.[57–59] We calculated the IR spectra that based on Enol, Enol*, and Keto* forms in Fig. 4. In detail, the O1–

H1 stretching vibrational frequency displays the characteristic peak at around 3040 cm^{-1} in the Enol* form. It is noteworthy that the characteristic peak around 3040 cm^{-1} disappears in the Keto* form, where a new characteristic peak attributed to N1–H1 emerges around 3410 cm^{-1}. It is evident that during the transition from Enol* to Keto*, the O1–H1 bond breaks, and the proton transfers from O1 to N1, forming N1–H1. Consequently, hydrogen bonding (O1$\cdots$H1–N1) exists within the Keto* form, as depicted in Fig. 2. Therefore, IR spectra can be effectively correlated with the result of proton transfer from O1 to N1, and serve as the dependable evidence of the proton transfer process.

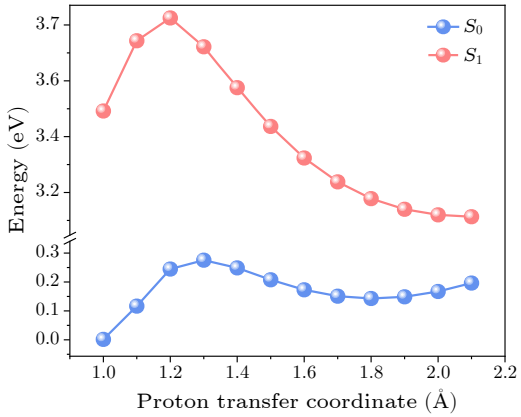

Fig. 3. PECs in the S_0 and S_1 states for BrA-HBI.

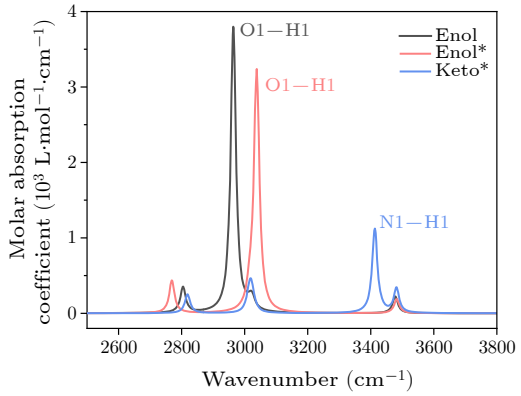

Fig. 4. Calculated infrared (IR) spectra of BrAHBI in the S_0 (Enol form) and S_1 states (Enol* form and Keto* form).

To predict the time scale of ESIPT, we calculated the proton transfer rate of k_{esipt} [60] via the transition state theory (TST),[60–62]

$$k_{esipt} = \frac{k_B T}{h} \exp\left(\frac{-\Delta G^{\ddagger}}{RT}\right), \tag{2}$$

where k_B is the Boltzmann constant, h is the Planck constant, R is the universal gas constant, $\Delta G^{\ddagger}$ from the Enol* to geometry of the TS point along the reaction path in the S_1 state. The Gibbs free energy is calculated by

$$\begin{aligned}\Delta G^{\ddagger} &= \Delta E + \Delta H^{\ddagger} - T\Delta S^{\ddagger} \\ &= \Delta E + \Delta H_{TS} - \Delta H_{Enol^*} - T(\Delta S_{TS} - \Delta S_{Enol^*}),\end{aligned} \tag{3}$$

where ΔE is the relative energy between the structure of TS and the Enol* form in the S_1 state, ΔH_{TS} and ΔH_{Enol^*} are the enthalpies on the TS and S_1 Enol* form, respectively, and ΔS_{TS} and $\Delta S_{S1\,Enol*}$ are the entropies on the TS and S_1 Enol* form, T is the temperature equal to 298 K. In addition, we calculated the relative energies, enthalpy corrections, and entropies for the S_1 Enol* and TS separately as shown in Table 1. The Gibbs free energy $\Delta G^{\ddagger} = 0.877$ kcal/mol and the rate $k_{esipt} = 1.409 \times 10^{12}\ s^{-1}$ were calculated. The calculated time scale for proton transfer (τ_{esipt}) is 709.554×10^{-15} s, indicating that it occurs within hundreds of femtoseconds, consistent with the general proton transfer time scale.

Table 1. Thermochemical data of BrA-HBI molecules obtained by computational analysis.

Structure	S_1 (Enol*)	TS
Relative energy (eV)[a]	0.000	0.161
Enthalpy correction (kcal/mol)	130.797	127.765
Entropy (cal·mol^{-1}·K^{-1})	123.137	122.434
$\Delta G^{\ddagger}$ (kcal/mol)	0.877	
k_{nr}^{MECI} (s^{-1})	1.409×10^{12}	
τ_{esipt} (s)	709.554×10^{-15}	

[a]The energy of the S_1 Enol* structure is set to 0.

TADF Mechanism. To clarify the TADF mechanism in the Keto* form, Table 2 lists the energy level gaps and spin-orbit coupling constants. The energy level gaps for S_1–T_1 and S_1–T_2 are 0.683 eV and 0.016 eV, respectively. The SOC_{ISC} constants of S_1–T_1 and S_1–T_2 are 38.048 cm^{-1} and 113.141 cm^{-1}, respectively. The process of ISC is characterized by the transition from the S_1 state to the T_1 state and the S_1 state to the T_2 state, and it is apparent that both transitions are possible. The SOC_{RISC} constants of T_2–S_1 and T_1–S_1 are 33.708 cm^{-1} and 2.855 cm^{-1}, respectively. It is obvious that the SOC_{RISC} constants of T_2–S_1 is larger than those of T_1–S_1 and the energy level gap of S_1–T_2 is smaller than that of S_1–T_1, which makes it easy to induce the RISC process from T_2 to S_1. Additionally, the reorganization energies are calculated.[63] The λ_S between S_1 and T_1 is 0.170 eV, which is smaller than that between S_1 and T_2 (0.567 eV). The λ_T between S_1 and T_1 is 0.207 eV, which is smaller than that between S_1 and T_2 (0.671 eV).

In order to discuss the TADF in more detail, the ISC and RISC rates of the BrA-HBI molecule in the Keto* form are also presented in Table 2. We calculated the classical Marcus rate equation[64] to obtain the rate of ISC and RISC, as specified in the Supporting Information (SI). The ISC rates of S_1–T_1 and S_1–T_2 were calculated to be $7.757 \times 10^{10}\ s^{-1}$ and $3.211 \times 10^{10}\ s^{-1}$, respectively. The transition rates for S_1–T_2 and S_1–T_1 are similar, with the extent of the reactions being nearly identical. Undoubtedly, both transitions are feasible. While the RISC rates for T_1–S_1 and T_2–S_1 are $6.358 \times 10^{1}\ s^{-1}$ and $6.900 \times 10^{9}\ s^{-1}$, respectively, the RISC rate for T_2–S_1 is 8 orders of magnitude higher than that for T_1–S_1. The data reveal that the RISC process from T_2 to S_1 significantly contributes to TADF.

Table 2. Calculated data obtained for the energy polarization, spin-orbit coupling matrix element (SOC), reorganization energy (λ) and reaction rate of BrA-HBI molecule in the Keto* form. Here, SOC_{ISC} is based on the optimized structures of single excited states, and SOC_{RISC} is based on the optimized structures of triplet excited states.

	ΔE (eV)	SOC_{ISC} (cm^{-1})	SOC_{RISC} (cm^{-1})	λ_S (eV)	λ_T (eV)	K_{ISC} (s^{-1})	K_{RISC} (s^{-1})
S_1–T_2	0.016	113.141	33.708	0.567	0.671	3.211×10^{10}	6.900×10^{9}
S_1–T_1	0.683	38.048	2.855	0.170	0.207	7.757×10^{10}	6.358×10^{1}

Consequently, by considering the energy gap, SOC constants of spin-orbit coupling reactions and transition rates, it is confirmed that the T_2 state plays a dominant role in the TADF phenomenon.

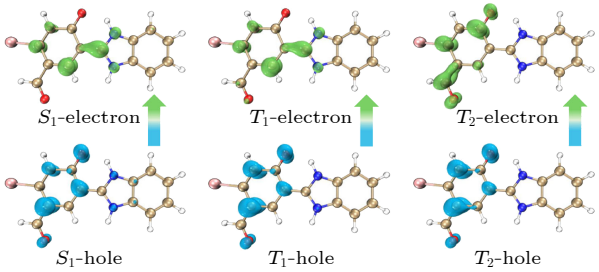

Fig. 5. Electron–hole distribution of BrA-HBI molecules in the S_1, T_1, and T_2 states, respectively, with green color representing electrons and blue color representing holes.

To explore the reason behind the T_2 state's predominant role in the TADF phenomenon, the electron–hole distribution schemes for the S_1, T_1, and T_2 states in Keto* form are illustrated in Fig. 5. The electron–hole distributions of the S_1 and T_1 states demonstrate significant spatial separation, indicating a propensity for charge transfer (CT) in both states. In contrast, the electrons and holes of the T_2 state are spatially similar, indicating a local excited (LE) state. It is evident that the electron–hole distribution of the T_2 state differs significantly from that of the T_1 and S_1 states. This disparity in electron–hole distribution results in a greater difference in the transition properties between the singlet and triplet states, thereby increasing the spin-orbit coupling.[65] This is the reason for the primary role of the T_2 state in the TADF phenomenon.

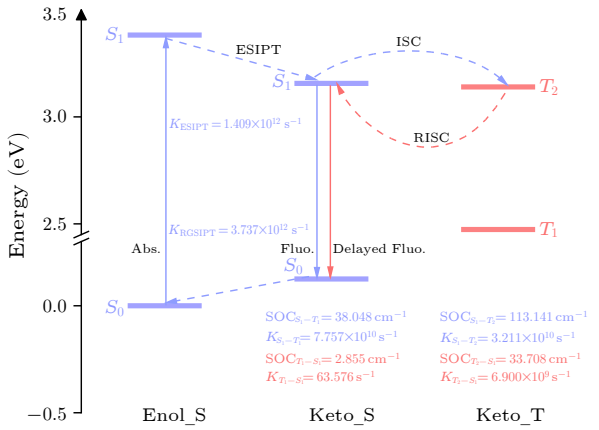

Fig. 6. Schematic diagram of luminescence processes for BrAHBI.

We have summarized the energy level diagrams of the singlet and triplet states of the BrA-HBI molecule, along with the photophysical processes of the TADF phenomenon and the ESIPT features, in Fig. 6. Upon excitation to the S_1 state, the BrA-HBI molecule undergoes intramolecular proton transfer, resulting in the formation of the S_1 Keto* structure. Subsequently, the prompt fluorescence emitted by the S_1 Keto* conformation competes with the efficient ISC from S_1 Keto* to T_2 Keto*. Thereafter, the T_2 state transitions to the S_1 state via the RISC process. Eventually, The S_1 Keto* form eventually decays to the S_0 Keto form through delayed fluorescence emission.

To enhance the accuracy of tuned range-separation functionals in predicting the TADF mechanism, we used double hybrid density functionals to calculate the singlet-triplet state energy level gaps (ΔE_{ST}) in the Keto* form.[36,37] As shown in Table 3, we have selected the representative SCS-ωB2GP-PLYP, SCS-ωPBEPP86, and SCS-ωB88PP86 functionals,[36–38] which have been demonstrated to be accurate and robust in predicting the TADF properties of organic molecules. The ΔE_{ST} calculated with double hybrid density functionals is consistent with our calculations utilizing optimally tuned range-separated functionals. Therefore, it is effective to calculate TADF properties of the BrA-HBI molecule utilizing the optimally tuned range-separated functionals.

Table 3. Energy difference between S_1 and T_2 states in the Keto* form of the BrA-HBI molecule under double hybridization calculations.

S_1–T_2	ΔE_{ST} (eV)
ωB97X*	0.016
SCS-ωB2GP-PLYP	0.026
SCS-ωPBEPP86	0.046
SCS-ωB88PP86	0.021

In conclusions, we decipher the TADF mechanism in metal-free organic emitter BrA-HBI molecules, utilizing the optimally tuned range-separation functionals for in-depth analysis. The ESIPT property of the BrA-HBI molecule was demonstrated by calculating its geometric structure, FMOs, PECs and IR spectra. In the calculation of the FMOs, it was discovered that the electrons in Keto* form of the molecule exhibit strong overlap of HOMO and LUMO, resulting in pronounced luminescence. The fluorescence quenching of the Enol* form is caused by the weak degree of frontier molecular orbital overlap between HOMO and LUMO, resulting in negligible oscillator strength. The transition state (TS) theory was employed to ascertain that the proton transfer process for this molecule takes place within hundreds of femtoseconds. By evaluating the SOCs, energy level gaps, non-radiative decay rates, and electron–hole distributions, we ascertained that the T_2 state is essential to the TADF phenomenon. To

further verify the reliability of the optimally tuned range-separation functionals on calculating the TADF mechanism, we adopted the double hybrid density functionals method to calculate the singlet-triplet energy gaps. The application of optimally tuned range-separated functionals to assess TADF properties aids in paving the way for highly efficient organic light-emitting diodes and enhancements in data encryption, solid-state lighting, and sensing technologies.

Acknowledgement. This work was supported by the National Natural Science Foundation of China (Grant No. 12174149)

References

[1] Shao W H, Hao J, Jiang H J, Zimmerman P M, and Kim J 2022 *Adv. Funct. Mater.* **32** 2201256
[2] Bryden M A and Zysman-Colman E 2021 *Chem. Soc. Rev* **50** 7587
[3] An Z F, Zheng C, Tao Y, Chen R F, Shi H F, Chen T, Wang Z X *et al.* 2015 *Nat. Mater.* **14** 685
[4] Fang F, Zhu L, Li M, Song Y Y, Sun M, Zhao D X, and Zhang J F 2021 *Adv. Sci.* **8** 2102970
[5] Chen X K, Zhang S F, Fan J X, and Ren A M 2015 *J. Phys. Chem. C* **119** 9728
[6] Long Y, Mamada M, Li C Y, dos Santos P L, Colella M, Danos A, Adachi C *et al.* 2020 *J. Phys. Chem. Lett.* **11** 3305
[7] Wu K L, Zhang T, Wang Z A, Wang L, Zhan L S, Gong S L, Zhong C *et al.* 2018 *J. Am. Chem. Soc.* **140** 8877
[8] Jiang G Y, Li F Y, Fan J Z, Song Y Z, Wang C K, and Lin L L 2020 *J. Mater. Chem. C* **8** 98
[9] Zhang W T, Yin H, Guo J, Zhao X, and Shi Y 2024 *Spectrochim. Acta Part A: Mol. Biomol. Spectrosc.* **304** 123319
[10] Jiang K 2023 *Chin. Phys. Lett.* **40** 017102
[11] Wu Y B, Wang R X, Lin R, Xu X, Zhang X, Osamah A, Qiu Y *et al.* 2023 *Chem. Eng. J.* **465** 142929
[12] Wang Y C, Jiang Y H, Wang G Q, Liu D J, Li B, and Hua J L 2015 *Chin. Phys. Lett.* **32** 048201
[13] Mamada M, Inada K, Komino T, Potscavage W J, Nakanotani H, and Adachi C 2017 *ACS Cent. Sci.* **3** 769
[14] Kwon J E and Park S Y 2011 *Adv. Mater.* **23** 3615
[15] Sedgwick A C, Wu L L, Han H H *et al.* 2018 *Chem. Soc. Rev.* **47** 8842
[16] Guo M L, Li Q, Yan L, Wan Y F, Zhu L X, Li B, Yin H *et al.* 2023 *Spectrochim. Acta Part A: Mol. Biomol. Spectrosc.* **300** 122937
[17] Kim H S, Lee J Y, Shin S, Jeong W, Lee S H, Kim S, Lee J *et al.* 2021 *Adv. Funct. Mater.* **31** 2104646
[18] Li X P, Baryshnikov G, Ding L J, Bao X Y, Li X, Lu J J, Liu M Q *et al.* 2020 *Angew. Chem. Int. Ed.* **59** 7548
[19] Jia H R, Wang Z B, Yuan T, Yuan F L, Li X H, Li Y C, Tan Z A *et al.* 2019 *Adv. Sci.* **6** 1900397
[20] Ahn D H, Kim S W, Lee H, Ko I J, Karthik D, Lee J Y, and Kwon J H 2019 *Nat. Photon.* **13** 540
[21] Sun H T, Zhong C, and Brédas J L 2015 *J. Chem. Theory Comput.* **11** 3851
[22] Dias F B, Penfold T J, and Monkman A P 2017 *Methods Appl. Fluoresc.* **5** 012001
[23] Autschbach J 2009 *ChemPhysChem* **10** 1757
[24] He X and Wang F 2006 *Chin. Phys. Lett.* **23** 1738
[25] Zhang H H, Yu W D, Gao C Z, and Qu Y Z 2023 *Chin. Phys. Lett.* **40** 043101
[26] Guo S D 2014 *Chin. Phys. Lett.* **31** 017101
[27] Varsano D, Di Felice R, Marques M A L, and Rubio A 2006 *J. Phys. Chem. B* **110** 7129
[28] Tawada Y, Tsuneda T, Yanagisawa S, Yanai T, and Hirao K 2004 *J. Chem. Phys.* **120** 8425
[29] Yanai T, Tew D P, and Handy N C 2004 *Chem. Phys. Lett.* **393** 51
[30] Körzdörfer T and Brédas J L 2014 *Accounts Chem. Res.* **47** 3284
[31] Baer R, Livshits E, and Salzner U 2010 *Ann. Rev.* **61** 85
[32] Autschbach J and Srebro M 2014 *Accounts Chem. Res.* **47** 2592
[33] Moore B and Autschbach J 2012 *Chemistryopen* **1** 184
[34] Adamo C and Barone V 1999 *J. Chem. Phys.* **110** 6158
[35] Sun H T, Hu Z B, Zhong C, Chen X K, Sun Z R, and Brédas J L 2017 *J. Phys. Chem. Lett.* **8** 2393
[36] Casanova-Páez M, Dardis M B, and Goerigk L 2019 *J. Chem. Theory Comput.* **15** 4735
[37] Casanova-Páez M and Goerigk L 2021 *J. Chem. Theory Comput.* **17** 5165
[38] Van Dijk J, Casanova-Páez M, and Goerigk L 2022 *ACS Phys. Chem. Au* **2** 407
[39] Frisch M J, Trucks G W, Schlegel H B *et al.* 2016 *Gaussian 16* Version B.01 (Wallingford: Gaussian, Inc.)
[40] Zhao X, Zhu L X, Li Q, Yin H, and Shi Y 2022 *Int. J. Mol. Sci.* **23** 13969
[41] Gao X, Bai S M, Fazzi D, Niehaus T, Barbatti M, and Thiel W 2017 *J. Chem. Theory Comput.* **13** 515
[42] Peng Q, Yi Y P, Shuai Z G, and Shao J S 2007 *J. Am. Chem. Soc.* **129** 9333
[43] Niu Y L, Li W Q, Peng Q *et al.* 2018 *Mol. Phys.* **116** 1078
[44] Niu Y, Peng Q, and Shuai Z 2008 *Sci. China Ser. B-Chem.* **51** 1153
[45] Escudero D 2016 *Accounts Chem. Res.* **49** 1816
[46] Neese F 2022 *Wires Comput. Mol. Sci.* **12** e1606
[47] Chaudhary J, Aarzoo, Roy R, and Roy R K 2022 *J. Phys. Chem. A* **126** 5252
[48] Sun H T, and Autschbach J 2014 *J. Chem. Theory Comput.* **10** 1035
[49] Sun H T, Zhang S A, and Sun Z R 2015 *Phys. Chem. Chem. Phys.* **17** 4337
[50] Mathivanan M and Murugesapandian B 2022 *Dyes Pigments* **203** 110367
[51] Yin H, Zhang Y M, Zhao H F, Yang G J, Shi Y, Zhang S X A, and Ding D J 2018 *Dyes Pigments* **159** 506
[52] Lin L L, Fan J Z, Cai L, and Wang C K 2017 *RSC Adv.* **7** 44089
[53] Yin H, Shi Y, and Wang Y 2014 *Spectrochim. Acta Part A: Mol. Biomol. Spectrosc.* **129** 280
[54] Mane S K B, Mu Y, Yang Z, Ubba E, Shaishta N, and Chi Z 2019 *J. Mater. Chem. C* **7** 3522
[55] Park H J, Lee H L, Lee H J, Lee K H, Lee J Y, and Hong W P 2019 *Chem. Mater.* **31** 10023
[56] Guo J, Yin H, Zhang W T, Zhao X, Zhao H F, and Shi Y 2023 *Dyes Pigments* **219** 111601
[57] Biswas A and Mallik B S 2022 *J. Mol. Liq.* **348** 118390
[58] Oparin R D and Kiselev M G 2024 *J. Mol. Liq.* **396** 123916
[59] Sun C, Zhao H, Liu X, Yin H, and Shi Y 2018 *Org. Chem. Front.* **5** 3435
[60] Ou Q, Peng Q, and Shuai Z G 2020 *J. Phys. Chem. Lett.* **11** 7790
[61] Peng Q and Shuai Z G 2021 *Aggregate* **2** e91
[62] Yin P A, Ou Q, Peng Q, and Shuai Z G 2023 *Aggregate* **4** e291
[63] Liu J, Fan J Z, Zhang K, Zhang Y C, Wang C K, and Lin L L 2020 *Chin. Phys. B* **29** 088504
[64] Vahtras O, Ågren H, Jørgensen P, Jensen H J A, Helgaker T, and Olsen J 1992 *J. Chem. Phys.* **97** 9178
[65] Chen X K, Kim D, and Brédas J L 2018 *Accounts Chem. Res.* **51** 2215